

Efficient use of an improved radiative transfer code to simulate near-global distributions of satellite-measured radiances

Takashi Y. Nakajima, Hiroshi Murakami, Masahiro Hori, Teruyuki Nakajima, Teruo Aoki, Tomohiko Oishi, and Akihiko Tanaka

Two new extension modules that give the water-leaving radiance from the ocean and the snow bidirectional reflectance distribution function were implemented in the latest radiative transfer code. In addition, to simulate the near-global distributions of satellite-measured radiances by using the improved radiative transfer code, we tested and applied the look-up table method together with the process-separation technique of the radiative transfer calculation. The computing time was reduced from 1 year to 20 s to simulate one channel, one scene of the Global Imager image by use of an Alpha 21164A-2 (600-MHz) machine. The error analyses showed that the radiances were simulated with less than 1% error for the nonabsorbing visible channels and ~2% error for absorbing channels by use of this method.

© 2003 Optical Society of America

OCIS codes: 010.1310, 120.0280.

1. Introduction

There has been an increasing number of studies and applications of satellite remote sensing to Earth observation.¹⁻³ These tendencies had been accelerated in this decade because the recent studies pertaining to global warming need both the general circulation model (GCM), which predicts the Earth's climate in the future, and the observed geophysical parameters for a global scale that validate the output characteristics obtained from the GCM. From this

point of view, the satellites' observations meet the global-scale acquisition of such geophysical parameters because of their suitable time and spatial resolution.

The satellite remote-sensing technique is based on the radiative transfer calculation, which simulates measured radiance of the sensors in orbit. It is required that the radiative scattering models of the target's geophysical parameters are included in the radiative transfer code used for such simulations. If the radiative transfer code has sensor-dependent engineering information, such as the response function of each channel and the orbital parameters of the satellite, this system will be called a software simulator for a sensor. In this paper, engineering information on the Global Imager (GLI) aboard the Advanced Earth Observing Satellite II (ADEOS-II) was given to the radiative transfer code. We call this software simulator the GLI Signal Simulator (GSS). The GSS makes it possible for us to optimize the channel design of satelliteborne radiometers in a purely theoretical manner. For example, Nakajima *et al.*⁴ optimized the GLI channel specifications to investigate the influence of water-vapor absorption and sensitivity for the target matters by using the previous version of the GSS. If the radiative transfer code has more scattering models of the geophysical parameters, such an improved code will have more technical merits for this purpose.

T. Y. Nakajima (nakajima@eorc.nasda.go.jp), H. Murakami, and M. Hori are with the Earth Observation Research Center, National Space Development Agency of Japan, Harumi Island Triton Square, Office Tower X 22F, 1-8-10 Harumi, Chuo-ku, Tokyo 104-6023, Japan. T. Nakajima is with the Center for Climate System Research, University of Tokyo, 4-6-1 Komaba, Meguro-ku, Tokyo 153-8904, Japan. T. Aoki is with the Department of Physical Meteorology Research, Meteorological Research Institute, 1-1 Nagamine, Tsukuba-shi, Ibaraki-ken 305-0052, Japan. T. Oishi is with the School of Marine Science and Technology, Tokai University, 2-15 Natsushima, Yokosuka, Kanagawa 237-0061, Japan. A. Tanaka is with Nagasaki Industrial Promotion Foundation, Nagasaki University, 1-14, Bunkyo-cho, Nagasaki-shi, Nagasaki 852-8521, Japan.

Received 18 July 2002; revised manuscript received 20 March 2003.

0003-6935/03/183460-12\$15.00/0

© 2003 Optical Society of America

Table 1. Summary of Final Specifications of the GLI Channels

Number	Wavelength (nm)	Bandwidth (nm)	Instantaneous Field of View (m/rad)	Condition				Target
				O	G	A	C	
1	380	10	1000/1.25	O	—	O	O	Absorption by DOM
2	400	10	1000/1.25	O	—	—	—	Baseline, DOM
3	412	10	1000/1.25	O	—	—	—	Absorption by chlorophyll, DOM
4	443	10	1000/1.25	O	O	O	O	Absorption by chlorophyll <i>a</i>
5	460	10	1000/1.25	O	O	O	O	Absorption by carotenoid
6	490	10	1000/1.25	O	—	—	—	Carotenoid, phycobiline
7	520	10	1000/1.25	O	—	O	O	Pigment
8	545	10	1000/1.25	O	O	O	O	Absorption by phycobiline
9	565	10	1000/1.25	O	—	—	—	Fluorescence minimum absorption
10	625	10	1000/1.25	O	—	—	—	Phycobiline, etc.
11	666	10	1000/1.25	O	—	—	—	Baseline, atmospheric correction
12	680	10	1000/1.25	O	—	—	—	Natural fluorescence
13	678	10	1000/1.25	—	O	O	O	Absorption by chlorophyll
14	710	10	1000/1.25	O	—	—	—	Baseline of fluorescence
15	710	10	1000/1.25	—	O	O	O	Sea ice monitoring
16	749	10	1000/1.25	O	—	—	—	Atmospheric correction
17	763	8	1000/1.25	—	O	O	—	Oxygen absorption
18	865	20	1000/1.25	O	—	—	—	Atmospheric correction
19	865	10	1000/1.25	—	O	O	O	Cloud and aerosol optical thickness
20	460	70	250/0.3125	—	O	O	O	Vegetation classification
21	545	50	250/0.3125	—	O	O	O	Vegetation classification
22	660	60	250/0.3125	—	O	O	O	Vegetation classification
23	825	110	250/0.3125	—	O	O	O	Vegetation classification
24	1050	20	1000/1.25	—	O	O	O	Moisture, snow-ice
25	1135	70	1000/1.25	—	—	O	—	Absorption by water vapor
26	1240	20	1000/1.25	—	O	O	O	Moisture, snow-ice
27	1380	40	1000/1.25	—	—	O	—	Water vapor, upper cloud
28	1640	200	250/0.3125	—	O	O	O	Snow, cloud phase
29	2210	220	250/0.3125	—	O	O	O	Cloud microphysical properties
	(μm)	(μm)		—	—	—	—	
30	3.715	0.33	1000/1.25	O		O	O	Cloud, snow microphysical parameters
31	6.7	0.5	1000/1.25			O		Water vapor
32	7.3	0.5	1000/1.25			O		Water vapor
33	7.5	0.5	1000/1.25			O		Water vapor
34	8.6	0.5	1000/1.25	O	O	O	O	Water vapor, temperature
35	10.8	1.0	1000/1.25	O	O	O	O	Temperature
36	12.0	1.0	1000/1.25	O	O	O	O	Temperature

^aO, ocean; G, ground; A, atmosphere; C, cryosphere; DOM, dissolved organic matter.

In this paper we developed an improved radiative transfer code (the improved GSS) based on the R System for Transfer of Atmospheric Radiation—5b (RSTAR5b) developed by Nakajima and Tanaka.^{5,6} The improved GSS has two new extension modules that give water-leaving radiance from the ocean and the snow bidirectional reflectance distribution function, as well as the older modules of the ocean surface of the Nakajima and Tanaka method⁷ with Cox-Munk statistics and the Lambert surface for simulating the accurate radiance observed from visible-to-infrared spaceborne radiometers. In addition, we simulated the near-global distribution of GLI measured radiances for one of the applications by using the improved GSS. For this purpose, we tested the look-up table (LUT) method together with a technique of the radiative transfer calculation that separates the ground surface process from the total process, for a reduction of the computing time. This technique has been suggested by some previous pa-

pers^{8,9} but was applied to only a few Advanced Very High Resolution Radiometer (AVHRR) channels. We applied this technique to most of the GLI channels in this paper. Table 1 summarizes the specifications of the GLI's 36 channels. It shows the channel position, bandwidth, special resolution, and expected targets applicable to each GLI channel.

2. Extension Modules of the Radiative Transfer Code

A. Basic Radiative Transfer Code, RSTAR5b

The RSTAR5b code uses the discrete ordinates method (DOM), with an extension for thermal radiation source terms as proposed by Stamnes *et al.*¹⁰ and for one or all of the Air Force Geophysics Laboratory's¹¹ six atmospheric models (tropical atmosphere, midlatitude summer, 1976 U.S. Standard, subarctic summer, midlatitude winter, and subarctic winter) that can be set in the simulations. The RSTAR5b had been equipped with radiative processes of ocean surface re-

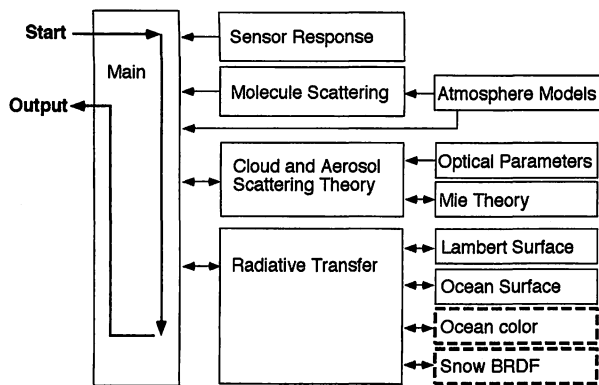


Fig. 1. Illustration of the improved RSTAR5b structure. Two extension modules (dashed boxes) have been installed since Nakajima *et al.*⁴ RSTAR5b is a complex of software tools for radiative transfer and optical modeling of the atmosphere.

reflection, the Lambert ground surface reflection, and the light-scattering process of atmospheric clouds and aerosols, with a highly systemized user interface of their optical and microphysical properties' settings. RSTAR5b calculates the expected measured radiance at the top of atmosphere (TOA) at any visible-to-infrared spaceborne sensor's channels accounting for sensor response functions. The structure of the improved RSTAR5b is shown in Fig. 1.

B. Extension Module of Water-Leaving Radiance by Ocean Colors

We installed an extension module for an ocean color process in RSTAR5b in this research. The module were developed by Tanaka *et al.*¹² on the basis of the simple radiative transfer model developed by Doerfer,¹³ which was described by Joseph's two-flow model.¹⁴ Joseph's two-flow model is expressed by optical parameters, i.e., the absorption coefficient and the backscattering coefficient. This module converts concentration of chlorophyll *a* (milligrams per cubic meter), dissolved organic matter (milligrams per liter), and suspended matter (1/m) to the water-leaving radiance (watts per square meter per steradians per micrometers) at GLI visible channels. Water-leaving radiance was added to the source matrix that presents the radiance interaction at the boundary layer in RSTAR5b. Two executions of RSTAR5b are needed to calculate the ocean color contributions: the first time for calculating the downward flux at the boundary layer without ground surface interaction and the second time for calculating the upward TOA radiance with the total process of radiative transfer. Figure 2 illustrates a difference in the expected measured radiance at the TOA with and without the ocean color contribution calculated by the improved RSTAR5b, as a function of 15 GLI ocean color channels in the visible at several satellite zenith angles θ . The boundary conditions were a solar zenith angle $\theta_0 = 45$ deg, a relative azimuth angle $\phi = 0$ deg, wind speed at 10 m above the ocean surface $u_{10} = 0.1$ m/s, and a chlorophyll-*a* concentration of 1.0 mg/m^3 . At the sat-

ellite zenith angle of $\theta = 45$ deg the difference in radiance seemed almost zero because a large reflection by Sun glint made the ocean color contributions small. The contribution increased with increasing u_{10} because the Sun glint decreased.

C. Extension Module of Snow Bidirectional Reflectance Distribution Function

This developed module converts snow grain size (micrometers) and snow impurity (parts per million by weight) into the bidirectional reflectance distribution function of the snow surface at every GLI wavelength from the visible to short-wave infrared. The reflectances of snow for various combinations of angles (solar and sensor zenith and azimuth angles) were calculated with a radiative transfer model. The model was based on the Mie (spherical) theory for single scattering of ice and soot particles with an assumption of an external mixture in a homogeneous snow layer (Aoki *et al.*¹⁵) and a standard size distribution of the gamma type (Hansen¹⁶). For multiple scattering in the snow layer the doubling and adding method was employed in the model (the details of this model was described by Aoki *et al.*¹⁷ and Aoki *et al.*¹⁵). The calculated snow bidirectional reflectance distribution function was operated with the reflection matrix of the boundary-layer process in RSTAR5b. Figure 3 shows the expected measured radiance with the function of snow grain size (micrometers) and snow impurity (ppmw) corresponding to GLI channels 13 ($0.678 \text{ } \mu\text{m}$, top panels), 24 ($1.05 \text{ } \mu\text{m}$, middle panels), and 28 ($1.64 \text{ } \mu\text{m}$, bottom panels). The boundary conditions were solar zenith angle $\theta_0 = 70$ deg, satellite zenith angle $\theta = 30$ deg, and relative azimuth angle $\phi = 50$ deg. The expected measured radiance is more sensitive to snow grain size at a longer wavelength than at a shorter wavelength because of a large absorption of the ice particle.

3. Look-Up Table Method and the Process-Separation Technique for the Fast Radiative Transfer Calculation

To generate a globally synthesized remote-sensing data set, it is unrealistic for one to calculate the expected measured radiance at every pixel in the image with a set of realistic atmospheric and boundary conditions because of the recent comparatively slow computing in radiative transfer. For example, we will spend nearly a year to simulate only one channel, one scene (1276×1656 pixels) of a GLI image when we calculate radiances at every pixel by using an Alpha 21164A-2 (600-MHz) machine. This is quite unreasonable because the GLI acquires more than 200 scenes in a day. It will be a common technique to use a LUT that archives simulated radiances with a considerable preset of parameters to overcome this difficulty. However, we may add another technique to the LUT method for calculating radiative transfer more efficiently than with the LUT method alone because many kinds of geophysical parameter make the LUT size undesirably large.

We tested therefore a technique that separates the ground surface process to reduce the dimensions of

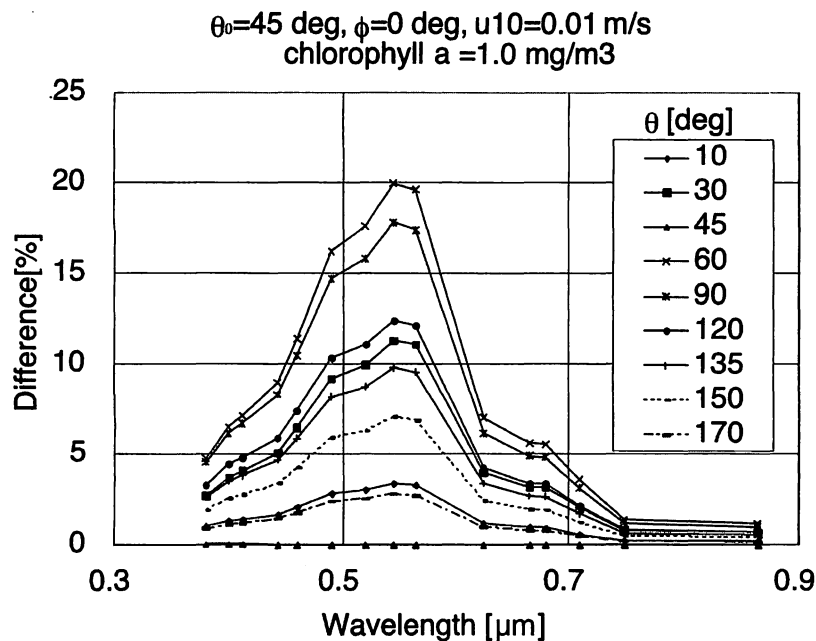


Fig. 2. Difference in expected measured radiance at the TOA, with and without ocean color contribution calculated by the improved RSTAR5b, at 15 GLI ocean color channels in the visible (see Table 1 for detailed channel positions).

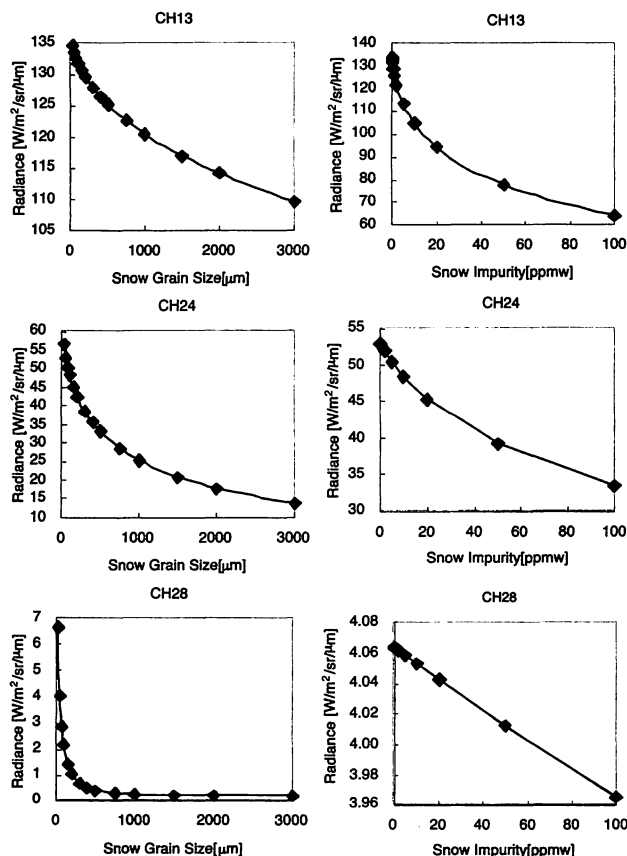


Fig. 3. Expected measured radiance with a function of snow grain size (micrometers) (left panels) and snow impurity (ppmw) (right panels) corresponding GLI channels 13 (0.678 μm , top panels), 24 (1.05 μm , middle panels), and 28 (1.64 μm , bottom panels). The solar zenith angle, satellite zenith angle, and relative azimuth angle were 70, 30, and 50 deg.

the LUT. Hereafter we call this procedure the process-separation technique. For example, when the atmospheric process in radiative transfer has four dimensions of $(\theta, \theta_0, \phi, \tau) =$ satellite zenith angle, solar zenith angle, relative azimuth angle, and optical thickness of the atmosphere and the ground surface process has two dimensions of $(A_g, T_g) =$ surface albedo and ground surface temperature, the maximum LUT dimension size of $4 + 2 = 6$ will be reduced to 4 by the process-separation technique. Moreover, when every dimension has ten discretized grid values, the total LUT size 10^6 will be reduced to only $10^4 + 10^2 \approx 10^4$ for this case. It is obvious that this technique is necessary for a global simulation of satellite-measured radiance because of the large variety of states of conditions in the Earth environment and numerous channels in current sensors. The principle of the process-separation technique was suggested and well examined by Kaufman and Nakajima⁸ and Nakajima and Nakajima⁹ for AVHRR's channels. For example, Nakajima and Nakajima⁹ applied this principle for the purpose of removing the radiative components (ground surface reflection and thermal emission) from the satellite-measured radiances to retrieve cloud-reflected solar radiance. In this paper, however, we apply this principle to compose TOA radiance from some separated radiative components. To examine the availability of this technique to cases other than the AVHRR case and to suggest some new formulations of the process separations are part of the principal goals in this paper.

Equations (1)–(6) are the formulations of the process-separation technique used to synthesize the GLI radiance (to avoid a long sentence in the text,

variables and parameters used in these formulations are summarized and explained in Table 2):

$$L_{\text{obs}}(\tau_c, r_e, z; \mu, \mu_0, \phi) = L_{\text{TOA_wos}}(\tau_c, r_e, z; \mu, \mu_0, \phi) + t(\tau_c, r_e, z; \mu) \frac{A_g}{1 - \bar{r}(\tau_c, r_e, z)A_g} \times t(\tau_c, r_e, z; \mu_0) \frac{\mu_0 F_0}{\pi}, \quad (1)$$

$$L_{\text{obs}}(\tau_a, \alpha; \mu, \mu_0, \phi) = L_{\text{TOA_wos}}(\tau_a, \alpha; \mu, \mu_0, \phi) + t(\tau_a, \alpha; \mu) \frac{A_g}{1 - \bar{r}(\tau_a, \alpha)A_g} \times t(\tau_a, \alpha; \mu_0) \frac{\mu_0 F_0}{\pi}, \quad (2)$$

$$L_{\text{obs}}(\tau_a, \alpha; \mu, \mu_0, \phi) = L_{\text{TOA_with_ocean}}(\tau_a, \alpha; \mu, \mu_0, \phi) + t(\tau_a, \alpha; \mu) Lw \mu_0 t(\tau_a, \alpha; \mu_0), \quad (3)$$

$$L_{\text{obs}}(\tau_c, r_e, z; \mu, \mu_0, \phi) = L_{\text{TOA_wos}}(\tau_c, r_e, z; \mu, \mu_0, \phi) + t(\tau_c, r_e, z; \mu) \frac{A_g}{1 - \bar{r}(\tau_c, r_e, z)A_g} \times t(\tau_c, r_e, z; \mu_0) \frac{\mu_0 F_0}{\pi} + t(\tau_c, r_e, z; \mu) \frac{1 - A_g}{1 - \bar{r}(\tau_c, r_e, z)A_g} B(T_g), \quad (4)$$

$$L_{\text{obs}}(\tau_a, \alpha; \mu, \mu_0, \phi) = L_{\text{TOA_wos}}(\tau_a, \alpha; \mu, \mu_0, \phi) + t(\tau_a, \alpha; \mu) \frac{A_g}{1 - \bar{r}(\tau_a, \alpha)A_g} \times t(\tau_a, \alpha; \mu_0) \frac{\mu_0 F_0}{\pi} + t(\tau_a, \alpha; \mu) \frac{1 - A_g}{1 - \bar{r}(\tau_a, \alpha)A_g} B(T_g), \quad (5)$$

$$L_{\text{obs}}(\tau_c, r_e, z; \mu) = L_{\text{TOA_wos}}(\tau_c, r_e, z; \mu) + t(\tau_c, r_e, z; \mu) \frac{1 - A_g}{1 - \bar{r}(\tau_c, r_e, z)A_g} B(T_g). \quad (6)$$

The left term in each formulation is the expected observed radiance. The first right term in Eqs. (1), (2), and (4)–(6) is the radiance at the TOA without land surface, and this term in Eq. (3) is the radiance at the TOA with ocean surface. The second and third terms are radiative components of the ground surface process. Equations (4) and (5), which are applied to the short-wave infrared channels, include both solar and thermal contributions at ground, whereas the solar or ocean color contributions to the visible to near-infrared channels are included in Eqs. (1)–(3), and only thermal contributions to the thermal infrared channels are included in Eq. (6). t is transmittance of atmosphere, and \bar{r} is a reflectance of the

Table 2. Explanations of Variables and Parameters in Eqs. (1)–(6)

Parameters	Explanation
L_{obs}	Satellite-measured radiance
$L_{\text{TOA_wos}}$	Simulated radiance at the TOA without surface
$L_{\text{TOA_with_ocean}}$	Simulated radiance at the TOA with the ocean surface
T	Transmissivity of atmosphere
\bar{r}	Spherical albedo
A_g	Ground albedo
T_g	Ground surface temperature
B	Planck function
F_0	Solar irradiance
Lw	Water-leaving radiance
τ_c	Cloud optical thickness
r_e	Cloud effective particle radius
z	Cloud-top height
τ_a	Aerosol optical thickness
α	Aerosol Ångström exponent
μ	Cosine of satellite zenith angle
μ_0	Cosine of solar zenith angle
ϕ	Relative azimuth angle

atmosphere illuminated from the bottom. For the case of cloud condition, they are expressed by

$$t(\tau_c, r_e; \mu_0) = \frac{1}{\pi} \int_0^{2\pi} \int_0^1 T(\tau_c, r_e; \mu, \mu_0, \phi) \mu d\mu d\phi + \exp(-\tau_c/\mu_0), \quad (7)$$

$$r(\tau_c, r_e; \mu) = \frac{1}{\pi} \int_0^{2\pi} \int_0^1 R(\tau_c, r_e; \mu', \mu, \phi) \mu' d\mu' d\phi, \quad (8)$$

$$\bar{r}(\tau_c, r_e) = 2 \int_0^1 r(\tau_c, r_e; \mu) \mu d\mu, \quad (9)$$

where $T(\tau, r_e; \mu, \mu_0, \phi)$ and $R(\tau, r_e; \mu', \mu, \phi)$ are bidirectional transmission and reflection functions, respectively. t and \bar{r} are averaged with the subchannel response function of GLI as

$$t = \frac{\sum_{n=1}^N \varphi_n \left[\sum_{k=1}^M (w_{n,k} t_{n,k}) \right]}{\sum_{n=1}^N \varphi_n}, \quad (10)$$

where φ_n is the response function of the n th subchannel wavelength for each GLI channel, $w_{n,k}$ is the weight of the k th k distribution, and $t_{n,k}$ is transmissivity for the k th k distribution at n th wavelength. This weighted averaging brings a nonnegligible error in the case that spectral variation of $t_{n,k}$ is large. The LUT becomes independent of ground surface temperature (T_g), water-leaving radiance (Lw), and ground albedo (A_g) (direct and diffused radiance are assumed to have the same reflectance at the ground) by the separation of the radiative process at the ground surface by use of these formulations.

Table 3. Summary of the Process-Separation Methods for Each Condition and GLI Channels

Condition	Channel						
	1–16, 18–23	24, 26, 28	17, 25, 27	29	30	31–34	35, 36
Cloud (L, O)	Eq. (1)	Eq. (1)	Lambert	Eq. (4)	Eq. (4)	Lambert	Eq. (6)
Aerosol (L)	Eq. (2)	Eq. (2)	Lambert	Eq. (5)	Lambert	Lambert	Lambert
Aerosol (O)	Ocean surface + Eq. (3)	Ocean surface	Ocean surface	Ocean surface	Ocean surface	Lambert	Lambert

^aL, land; O, ocean.

Table 3 summarizes the formulation number [Eqs. (1)–(6)] of the process separation applied to several atmospheric and ground conditions at each GLI channel. In some GLI channels, such as 17, 25, 27, and 31–34, no process separations were applied to all Earth environmental conditions because of the comparatively large absorption by the atmosphere that makes the radiative transfer more complicated. Figure 4 illustrates the compression ratio of the LUT size with and without this technique for each GLI channel. For most of the visible and short-wave infrared channels, the LUT size with the process-separation technique can be compressed by 13.6% compared with that without the process-separation technique. Ultimately, the computing time was reduced from a year to 20 s to simulate one channel, one scene of a GLI image by using an Alpha 21164A-2 (600-MHz) machine. This is reasonable for the global simulation even counting one day of computing time to generate a LUT for each channel.

4. Virtual Earth Environment

Use of satellite measurements, objective analysis, GCM outputs, or model-calculated values of geophysical parameters or all of these establishes a virtual Earth environment. Because the cloud parameters set in the virtual Earth environment were obtained from daytime satellite remote sensing that needed a sufficient solar reflectance from clouds, simulations were restricted only in the area of

60 °N < latitude < 60 °S. Table 4 summarizes the geophysical parameters and their sources. The following subsections explain the parameter settings.

A. Model Atmosphere and Surface Temperature

We used the 1976 U.S. Standard Atmosphere model in the near-global region for the atmospheric molecular profile and temperature profile for other than surface temperature. Objectively analyzed surface temperature data, from the Japan Meteorological Agency's Global Analysis, on 15 January 1999 were applied to a global distribution. Minimum and maximum values were 234.2 and 308.5 K. If the surface was identified to be water, such as oceans, great lakes, and rivers, we used the satellite remote-sensed values of water surface temperature obtained from the TRMM (Tropical Rainfall Measurement Mission) Microwave Imager aboard the TRMM satellite in January 1999. The minimum and maximum values of water surface temperature were 271.3 and 309.4 K.

B. Ocean Color Matters

Concentration of chlorophyll *a*, dissolved organic matter, and suspended matter retrieved from the Ocean Color and Temperature Scanner aboard the Advanced Earth Observing Satellite II were used

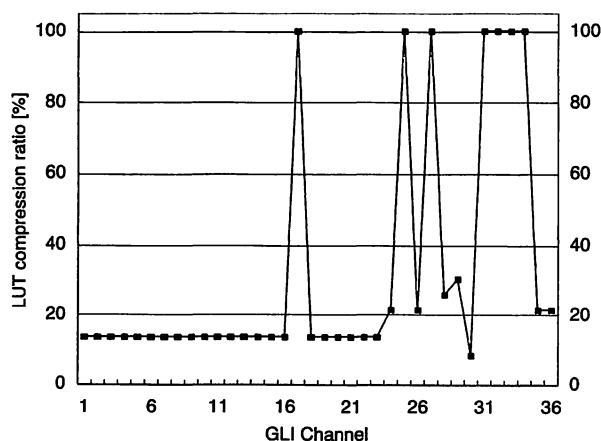


Fig. 4. Compression ratio of LUT size with and without this technique for each GLI channel. Specifications for each channel are summarized in Table 1.

Table 4. Summary of the Geophysical Parameters and Their Sources

Geophysical Parameters	Data Source
Model atmosphere	1976 U.S. Standard
Ground surface temperature (T_g)	Japan Meteorological Agency, Global Analysis
Sea surface temperature	TRMM Microwave Imager, TRMM
Ocean color matters	Ocean Color and Temperature Scanner, ADEOS
Land cover	AARS and ASTER Spectral Library
Aerosol optical thickness	CCSR-NIES GCM
Aerosol Ångström exponent	CCSR-NIES GCM
Snow cover	Near-real-time SSM/I
Snow grain size (r_s)	Eq. (12)
Snow impurity (ξ)	Eq. (13)
Cloud optical thickness	AVHRR, NOAA-11
Cloud effective particle radius	AVHRR, NOAA-11
Cloud-top temperature	AVHRR, NOAA-11

for input data for deriving the upwelling radiance L_w at the water surface.

C. Land-Cover Types and Their Reflectance

We used a simplified Asian Association on Remote Sensing (AARS) global 4-min land-cover data set^{18,19} for land-cover classification in our virtual Earth environment. Because only four types of reflectance data corresponding to grass, conifer, deciduous, and solid can clearly be set for GLI channels by using the Advanced Spaceborne Thermal Emission and Reflection Radiometer (ASTER) Spectral Library, we combined 56 types of land use in AARS into the four types above. The spectral reflectance for each land use was integrated by the response functions of GLI channels 1 (380 nm) to 30 (3.715 μm) for preparing the process separation. For the GLI channels longer than 6.0 μm (channels 31–36 of the GLI), the surface reflectance was set to zero.

D. Aerosol Distributions and Properties

Global distribution of the aerosol optical thickness τ_a and the angstrom exponent α of an aerosol model of a mixture of soil, dust, carbonaceous material, sulfate, and sea salt were simulated by the spectral radiation-transport model for aerosol species²⁰ (SPRINTARS) coupled with the GCM,²¹ which has been developed at the Center for Climate System Research (CCSR) of the University of Tokyo and the National Institute of Environmental Studies (NIES). These two aerosol parameters were input into the radiative transfer. A two-mode size distribution,

$$\frac{dV}{d \ln(r)} = \sum_{i=1}^2 \left(c_i \exp \left\{ -\frac{1}{2} \left[\frac{\ln(r/r_{mi})}{\ln(\sigma_i)} \right]^2 \right\} \right), \quad (11)$$

was applied to the aerosol size distribution, where C is a constant, r and r_m are the radius and mode radius (micrometers) of aerosol particles, and σ is the standard deviation of size distribution. We set $(C, r_m, \sigma) = (1.0, 0.17, 1.30)$ and $(C_2, 3.44, 2.75)$ for the first and second modes with a complex refractive index of $1.500 - i0.005$, where C_2 is a function of α . Maximum and minimum values for optical thickness and the Ångström exponent were $\text{Max} = 1.35$, $\text{Min} = 0.00153$, and $(0.8, 0.0007)$.

E. Snow-Cover Distributions and Properties

We used the near-real-time Special Sensor Microwave Imager (SSM/I) Equal-Area Scalable Earth Grid daily global ice concentration and snow-extent product of the National Snow and Ice Data Center's Distributed Active Archive Center data²² on 11 January 2000 for the snow-cover-area setting. We calculated the model snow grain size r_s as a function of ground surface temperature T_g and the model snow impurity ξ as a function of optical thickness of the sulfate aerosol τ_{sulfate} obtained by the CCSR-NIES

GCM. The formulas below calculate r_s (micrometers) and ξ (ppmw):

$$r_s = \exp \left[\frac{\ln(2000) - \ln(25)}{273.15 - 253.15} (T_g - 253.15) + 25.0 \right], \quad (12)$$

if $T_g < 253.15$, then $r_s = 25.0$ and if $T_g \geq 273.15$, then $r_s = 2000.0$, and

$$\xi = \frac{1 - 0.01}{0.005 - 1.63 \times 10^{-4}} (\tau_{\text{sulfate}} - 0.005) + 1.0, \quad (13)$$

if $\tau_{\text{sulfate}} \geq 0.01477$, $\xi = 3.0$.

Equation (12) is based on the assumption that snow grains grow from 25 μm in radius for new snow to 2000 μm for old snow near the melting point, sensitively depending on the ground surface temperature (T_g). For the relation between snow types and average grain radii, we refer to Wiscombe and Warren.²³ As to Eq. (13), snow impurity is mainly considered to be aerosol particles deposited from polluted air masses by a dry-deposition process. Thus we assumed that impurity concentration in the snow was linearly varied with that of sulfate aerosol, which could be a good index for the polluted atmosphere obtained by the SPRINTARS. For the case of Barrow in Alaska, U.S., the *in situ* measurement value (Aoki *et al.*²⁴), by use of ground optical observations and theoretical calculations, and the calculated value of the snow impurity were 0.1 and 0.17 ppmw, respectively. Validation of the adequacy for these assumptions will be done by future GLI measurements or other observations.

F. Warm Cloud Distribution and Properties

For optical and microphysical properties of warm clouds, such as cloud optical thickness τ_c , cloud effective particle radius r_e , and cloud-top temperature T_c , we used the one-month mean data derived from the AVHRR aboard the NOAA-11 (National Oceanic and Atmospheric Administration) measurements in January 1990.^{9,25} The region of latitude was limited to within 60 °N to 60 °S for cloud optical and microphysical properties because these parameters were retrieved by solar reflectance that was measured only in the daytime with a small solar zenith angle. To make the total global cloud area realistic, we neglected clouds that have an optical thickness less than 6. This threshold value is somewhat larger when we are reminded of studies of a global average of warm cloud optical thickness of 7 or 8, examined in past research.^{2,25} Therefore this simulation gives a feature of measured radiance under relatively thick warm clouds. This might be a better choice because, if we apply the cloud distribution obtained from the one-day data of the AVHRR in order to consider optical thickness from thin to moderate values, the simulation becomes far from that of the GLI owing to differences in orbit and swath between the AVHRR and the GLI. Moreover, the broken appearance of

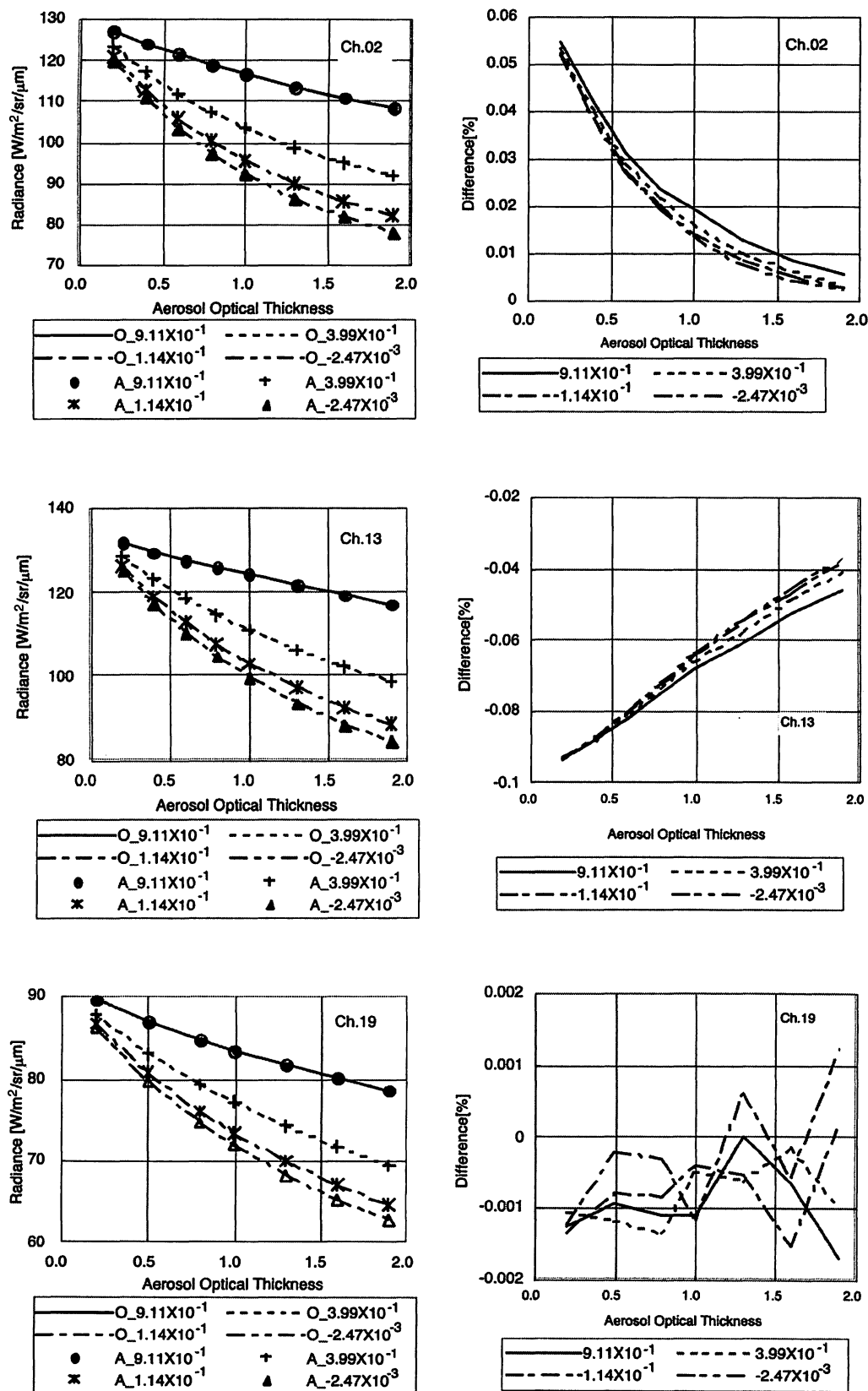


Fig. 5. Expected measured radiance (left panels) and the difference (%) (right panels) with and without the process-separation technique, with fixed ground albedo of 0.6, as a function of aerosol optical thickness at 500 nm with Ångström exponents of 9.11×10^{-1} , 3.99×10^{-1} , 1.14×10^{-1} , and -2.47×10^{-3} for GLI channels 2 ($0.400 \mu\text{m}$), 13 ($0.678 \mu\text{m}$), and 19 ($0.865 \mu\text{m}$). The scan geometries were $\theta_0 = 60$ deg, $\theta = 40$ deg, and $\phi = 50$ deg. O_- and A_- in the left panels' legends denote without and with the process-separation technique.

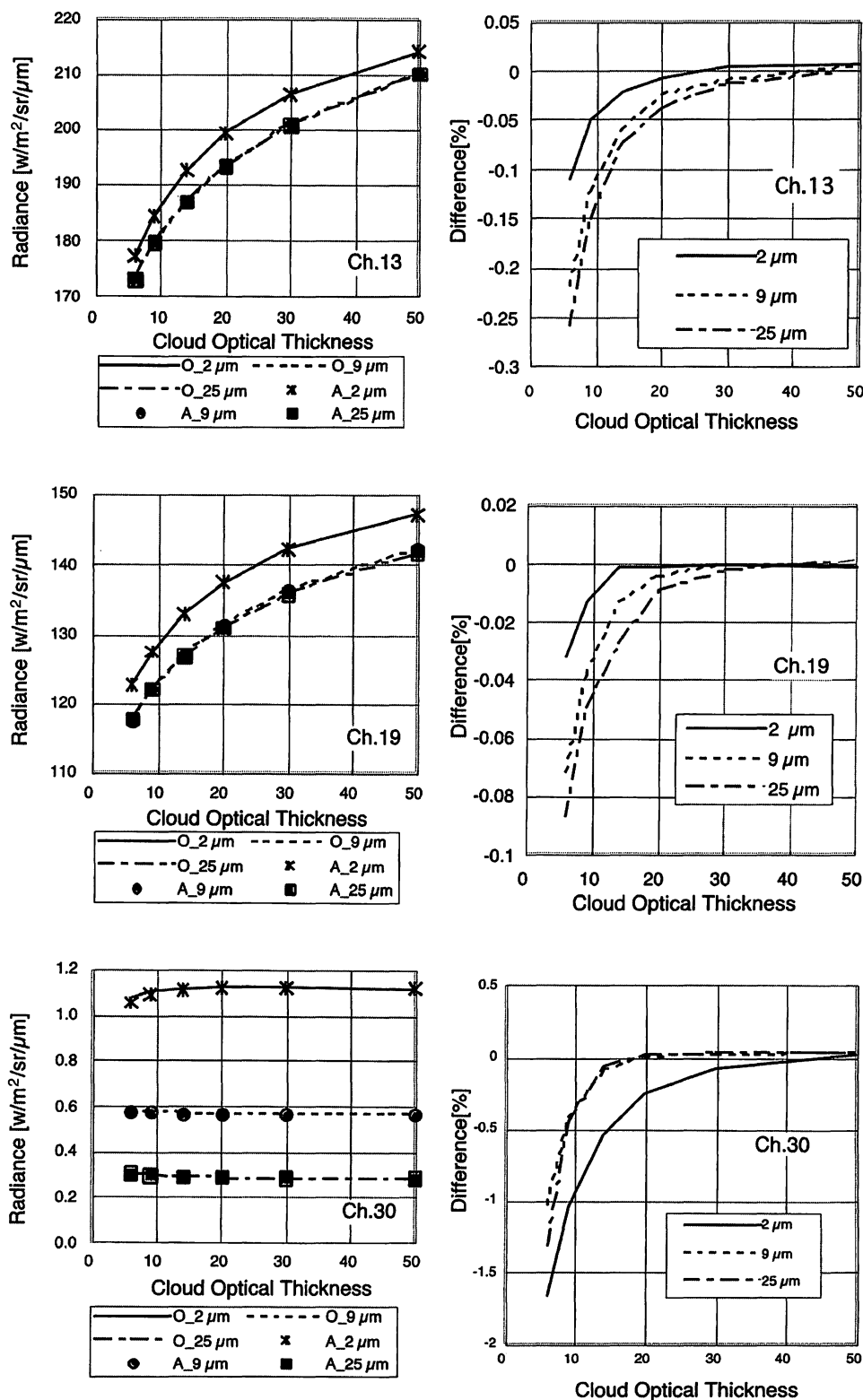


Fig. 6. Same as Fig. 5 but for GLI channels 13, 19, and 30, with clouds as a function of cloud optical thickness with effective particle radii of 2, 9, and 25 μm .

warm clouds in the one-day retrievals will also make the simulated image unnatural.

We did not account for any ice clouds in this examination because of the ambiguity of ice cloud distri-

butions and unsolved problems in light scattering by nonspherical particles, especially in a wavelength domain comparable with the size of the particle. This will be solved in future research.



Fig. 7. Red (0.678 μm), green (0.545 μm), and blue (0.400 μm) composite near-global image obtained by the virtual remote sensing of the GLI, corresponding to 15 Sun-synchronous orbits on 29 January 2001.

5. Results and Discussion

A. Accuracy of the Calculations

To examine the accuracy of the process-separation technique, we compare the expected measured radiance calculated with and without this technique.

1. Under Aerosol Conditions

Figure 5 illustrates the expected measured radiance (left panels) and the difference (percentage) (right panels) with and without the process-separation technique, with fixed ground albedo of 0.6, as a function of aerosol optical thickness at 500 nm with Ångström exponents of 9.11×10^{-1} , 3.99×10^{-1} , 1.14×10^{-1} , and -2.47×10^{-3} for GLI channels 2 (0.400 μm), 13 (0.678 μm), and 19 (0.865 μm). The scan geometries were $\theta_0 = 60$ deg, $\theta = 40$ deg, and $\phi = 50$ deg. O_- and A_- in the left panels' legends denote without and with the process-separation technique. We found good agreement in radiance with and without the process-separation technique; the differences were less than 1% for GLI channels 1–13, 16–22, and 24–26 but were somewhat larger for channels 14 (1.4%), 15 (1.3%), 23 (2%), 28 (1.2%), and 29 (2%), in which small but remarkable atmospheric absorptions were included in their response domain. In the shorter wavelengths, such as channel 2 (400 nm), both the Rayleigh scattering (at the aerosol layer) and the aerosol scattering affect t and \bar{r} calculations by Eq. (10). Because the spectral variation of $t_{n,k}$ by the n th subchannel is larger in Rayleigh scattering than in aerosol scattering, the error becomes small with a large aerosol optical thickness in this case. When the sensor response is narrower than the present value, this difference can be smaller than this result. This is a future engineering study for sensor designing. The difference decreased with decreasing solar and satellite zenith angles and decreasing ground albedo.

2. Under Cloud Condition

Figure 6 is the same as Fig. 5 but for GLI channels 13, 19, and 30 (3.715 μm), with clouds as a function of cloud optical thickness with effective particle radii $r_e = 2$, 9, and 25 μm . The process-separation technique works well for all channels because the cloud-reflected component of radiance is somewhat larger than that of aerosol so that possible errors become small enough to neglect. The differences were less than 1% for most GLI channels but larger for channels 1–15 and 30 (2%) especially in thin optical thickness. Channel 30's radiance seemed independent of cloud optical thickness but dependent on effective particle radius. This is the principle of effective radius retrieval by use of channel 30. The process-separation technique is suitable for simulation of expected measured radiance over cloud areas.

B. Global-Synthesized Observed Radiance for Three Major Global Imager Channels

Figure 7 illustrates a red (0.678 μm), green (0.545 μm), and blue (0.400 μm) composite image obtained by the virtual remote sensing of the GLI, corresponding to 15 Sun-synchronous orbits on 29 January 2001. The equator-crossing local time of each path is 10:30 a.m. We found a natural glance of an image over the Earth. Sun glints are represented in the midlatitude of the southern hemisphere over a cloud-free ocean area. Contrast in clouds, grassland, and desert is also represented. Small data gaps shown in every orbit are made by changing the sensor-tilting mode of the GLI operation. Figure 8 illustrates the spectral simulated radiance of a typical wavelength in the (a) near-infrared (0.865 μm), (b) short-wave infrared (3.715 μm), and (c) thermal infrared (10.8 μm) channels of the GLI. In Fig. 8(a) the simulated radiance is brighter over cloud and land areas than over the ocean area. It decreases with an increase in latitude because of the change in the solar zenith angle. Figure

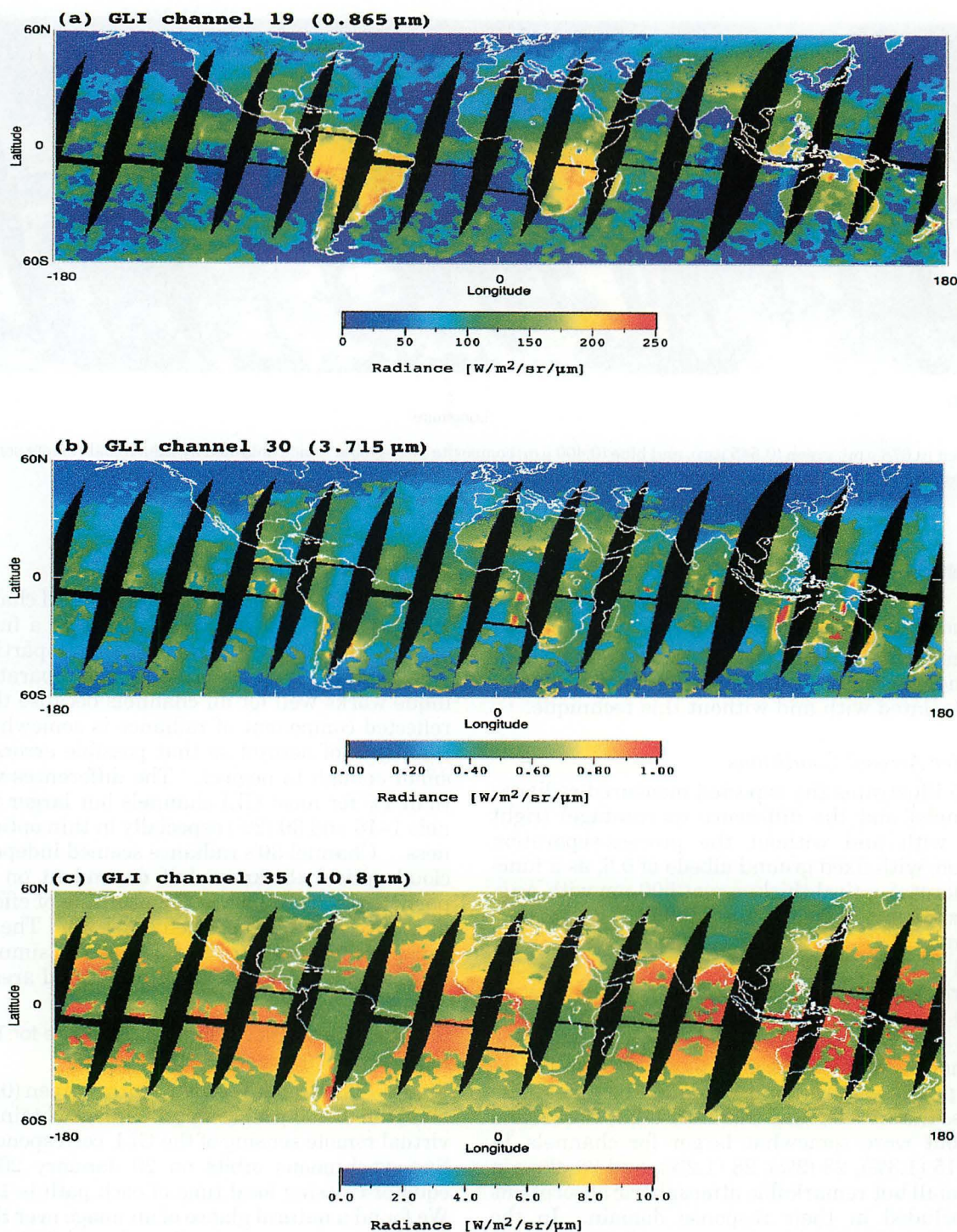


Fig. 8. Simulated radiance of typical wavelengths in (a) visible $0.865\ \mu\text{m}$, (b) short-wave infrared $3.715\ \mu\text{m}$, and (c) thermal infrared $10.8\ \mu\text{m}$ channels of the GLI.

8(b) is more ambiguous than Fig. 8(a) because this wavelength includes both thermal emission and solar-reflected components; observations of high-level thick clouds and low-level thin clouds can have almost the same radiance. Over middle-level moderately thick clouds, the thermal emission is approximately 30% of the total measured radiance. In Fig. 8(c) the measured radiance is smaller over clouds and a high-

latitude area than over midlatitude and low-latitude land owing to the difference in temperature.

6. Summary

Two newer modules developed by the GLI science project were implicitly installed in the latest radiative transfer code RSTAR5b, so that it became possible to calculate radiances in a land-to-atmosphere

system more complicated than before. We tested and applied the LUT method together with the process-separation technique, which separates the ground surface process in radiative transfer with high accuracy. This technique drastically reduced the LUT size so that virtually constructed Earth environments that have various states of condition can be remotely sensed by computer simulation.

The error analyses showed that the process-separation technique in radiative transfer worked very well for most GLI channels, especially for nonabsorbing visible channels (less than 1%). In contrast, for absorbing channels such as 17, 25, 27, and 31–34, the errors became large (~2%). Therefore we did not apply the process-separation technique to those cases. When the sensor response width is narrower than 10 nm, the error can also be small. This will be a future engineering study for sensor designing.

The authors are grateful to Yoshiaki Honda of Chiba University and Mitchell Verstraete of the Space Applications Institute for their valuable comments on land classifications and spectral reflection in the simulation, to Ryutaro Tateishi of Chiba University for providing an AARS global 4-min land-cover data set, and to Akiko Higurashi of the National Institute of Environmental Studies and Toshihiko Takemura of Kyushu University for providing the aerosol data set. The authors thank Hajime Fukushima of Tokai University and Motoaki Kishino for their support on the ocean characteristics setting. ASTER spectral data were reproduced from the ASTER Spectral Library through the courtesy of the Jet Propulsion Laboratory, California Institute of Technology. This research was partly supported by the GLI science project in the Earth Observation Research Center at the National Space Development Agency of Japan and Core Research for Evolutional Science and Technology at Japan Science and Technology Corporation.

References

- W. B. Rossow, "Measuring cloud properties from space: a review," *J. Clim.* **2**, 201–213 (1989).
- Q. Han, W. B. Rossow, and A. A. Lacis, "Near-global survey of effective droplet radii in liquid water clouds using ISCCP data," *J. Clim.* **7**, 465–497 (1994).
- A. Higurashi and T. Nakajima, "Development of a two channel aerosol retrieval algorithm on global scale using NOAA/AVHRR," *J. Atmos. Sci.* **56**, 924–941 (1999).
- T. Y. Nakajima, T. Nakajima, M. Nakajima, H. Fukushima, M. Kuji, A. Uchiyama, and M. Kishino, "Optimization of the Advanced Earth Observing Satellite II Global Imager channels by use of radiative transfer calculations," *Appl. Opt.* **37**, 3149–3163 (1998).
- T. Nakajima and M. Tanaka, "Matrix formulation for the transfer of solar radiation in a plane-parallel scattering atmosphere," *J. Quant. Spectrosc. Radiat. Transfer* **35**, 13–21 (1986).
- T. Nakajima and M. Tanaka, "Algorithms for radiative intensity calculations in moderately thick atmospheres using a truncation approximation," *J. Quant. Spectrosc. Radiat. Transfer* **40**, 51–69 (1988).
- T. Nakajima and M. Tanaka, "Effect of wind-generated waves on the transfer of solar radiation in the atmosphere-ocean system," *J. Quant. Spectrosc. Radiat. Transfer* **29**, 521–537 (1983).
- Y. Kaufman and T. Nakajima, "Effect of Amazon smoke on cloud microphysics and albedo—analysis from satellite imagery," *J. Appl. Meteorol.* **32**, 729–774 (1993).
- T. Y. Nakajima and T. Nakajima, "Wide-area determination of cloud microphysical properties from NOAA AVHRR measurements for FIRE and ASTEX regions," *J. Atmos. Sci.* **52**, 4043–4059 (1995).
- K. Stamnes, S.-C. Tsay, W. Wiscombe, and K. Jayaweera, "Numerically stable algorithm for discrete-ordinate-method radiative transfer in multiple scattering and emitting layered media," *Appl. Opt.* **27**, 2502–2509 (1988).
- F. X. Kneizys, E. P. Shettle, L. W. Arbeau, J. H. Chetwynd, G. P. Anderson, W. O. Gallery, J. E. A. Selby, and S. A. Clough, "Users guide to LOWTRAN-7," Tech. Rep. AFGL-TR-88-0177 (U.S. Air Force Geophysics Laboratory, Hanscom Air Force Base, Mass., 1988).
- A. Tanaka, T. Oishi, M. Kishino, and D. Roland, "Application of the neural network to OCTS data," presented at the Fourteenth Ocean Optics Conference, Kailua Kona, Hawaii, 10–13 November 1998.
- R. Doerffer, "Imaging spectroscopy for detection of chlorophyll and suspended matter," *Imaging Spectroscopy and Prospective Applications*, F. Toselli and J. Bodechtel, eds. (ECSC-EEC-EAEC, Brussels-Luxembourg, 1992) pp. 215–257.
- J. Joseph, "Untersuchungen über ober- und unterlichtmessungen im meere und über ihren zusammenhang mit durchsichtigkeitsmessungen," *Dtsch. Hydrogr. Z.* **3**, 324–335 (1950).
- T. Aoki, T. Aoki, M. Fukabori, A. Hachikubo, Y. Tachibana, and F. Nishio, "Effects of snow physical parameters on spectral albedo and bidirectional reflectance of snow surface," *J. Geophys. Res.* **105**, 10219–10236 (2000).
- J. E. Hansen, "Multiple scattering of polarized light in planetary atmospheres. Part II. Sunlight reflected by terrestrial water clouds," *J. Atmos. Sci.* **28**, 1400–1426 (1971).
- T. Aoki, T. Aoki, M. Fukabori, and A. Uchiyama, "Numerical simulation of atmospheric effects on snow albedo with a multiple scattering radiative transfer model for the atmosphere-snow system," *J. Meteorol. Soc. Jpn.* **77**, 595–614 (1999).
- P. A. Agbu and M. E. James, *The NOAA/NASA Pathfinder AVHRR Land Data Set User's Manual* (Goddard Distributed Active Center, NASA, Goddard Space Flight Center, Greenbelt, Md., 1994).
- S. W. Running, T. R. Loveland, and L. L. Pierce, "A vegetation classification logic based on remote sensing for use in global biogeochemical models," *Ambio* **23**, 77–81 (1994).
- T. Takemura, H. Okamoto, Y. Maruyama, A. Numaguti, A. Higurashi, and T. Nakajima, "Global three-dimensional simulation of aerosol optical thickness distribution of various origins," *J. Geophys. Res.* **105**, 17853–17873 (2000).
- A. Numaguti, "Dynamics and energy balance of the Hadley circulation and the tropical precipitation zones: significance of the distribution of evaporation," *J. Atmos. Sci.* **50**, 1874–1887 (1993).
- A. Nolin, R. L. Armstrong, and J. Maslanik, "Near real-time SSM/I EASE-grid daily global ice concentration and snow extent," National Snow and Ice Data Center, Boulder, Colo., data on 11 January 2000, digital media.
- W. J. Wiscombe and S. G. Warren, "A model for the spectral albedo of snow. I: Pure snow," *J. Atmos. Sci.* **37**, 2712–2733 (1980).
- T. Aoki, T. Aoki, M. Fukabori, Y. Tachibana, Y. Zaizen, F. Nishio, and T. Oishi, "Spectral albedo observation on the snow field at Barrow, Alaska," *Polar Meteorol. Glaciol.* **12**, 1–9 (1998).
- K. Kawamoto, T. Nakajima, and T. Y. Nakajima, "A global determination of cloud microphysics with AVHRR remote sensing," *J. Clim.* **14**, 2054–2068 (2001).